X-Ray Analysis of Active Galactic Nuclei in Clusters from the Dark Energy Survey

A Thesis Submitted in Partial Satisfaction
Of the Requirements for the Degree of
Bachelor of Science in Physics at
the
University of California, Santa Cruz

By
Erica M. Bufanda
May 16, 2015

_____	_____
Tesla Jeltema	Adriane Steinacker
Advisor	Senior Theses Coordinator

_____
Robert P. Johnson
Chair, Department of Physics

X-Ray Analysis of Active Galactic Nuclei in Clusters from the Dark Energy Survey

Erica Bufanda[1]

1. Department of Astronomy and Astrophysics, University of California, Santa Cruz

Abstract

We use Chandra X-ray images combined with optical information from the redMaPPer catalogue of clusters of galaxies detected by the Dark Energy Survey to analyze the evolution of Active Galactic Nuclei (AGN) and their host galaxies in large scale structure. Recent research has shown that the presence of AGN in clusters is a function of redshift and cluster richness. Our purpose is to investigate these correlations and what this implies for the evolution of AGN in clusters. We accumulated a sample of 141 AGN in 659 clusters at $0.2<z<1$ using an IDL matching program that matches the optical positions of galaxies in clusters detected in early data from the Dark Energy Survey (DES) redMaPPer cluster member catalogue v. 6.2.12 with the X-ray positions of detected point sources in 93 different Chandra X-ray observations. We identified each confirmed match with the imaging software Ds9 and calculated the X-ray count rate, flux, and luminosity of the point sources. We investigate the AGN fraction as a function of richness and redshift with a luminosity threshold of 10^{43} ergs/sec and selective richness and redshift cuts. We find that AGN in clusters of all richness increase by a factor of 8.8 from redshift 0.2 to 1. The high redshift AGN fraction is greater than the low redshift AGN fraction at 5σ. This is consistent with Martini et al's findings in 2009. The AGN fraction increases by a factor of 9.8 and 11.2 for AGN in clusters with low richness ($\lambda<25$) and high richness ($\lambda>25$) respectively. In addition the AGN fraction does not seem to have any significant dependence on cluster richness. This implies that AGN are equally as likely to be observed in galaxy groups as well as larger mass clusters. A larger sample of high and intermediate mass clusters could possibly verify this claim. Future work involves a recalculation of the AGN fraction and a reanalysis of our cluster AGN sample with the most current DES redMaPPer cluster catalogue.

1 Introduction

Galaxies are a key component in the formation of large scale structure (Planelles et al, 2014), however their origins and evolution on large time scales are elusive, debated, and complicated. Every massive galaxy detected is thought to have a supermassive black hole (SMBH) (Ford et al, 1998). Recent studies have shown that the size of this SMBH is correlated with various properties of its host galaxy, such as the velocity dispersion of the central bulge of that galaxy (Ferrarese &Merritt 2000; Gebhardt et al. 2000; Haehnelt et al, 2000; Tremaine et al. 2002; Graham, 2015) and central bulge formation (Xu et al, 2007; Graham 2015). Hence, one can infer that the evolution of the central SMBH and its host galaxy are intimately connected.

The central SMBH in every galaxy is observed to be either dormant or active, where the former refers to a galaxy that has a relatively quiescent black hole that is not accreting matter. Active SMBH in galaxies are known as active galactic nuclei (AGN). They are accreting mass from the central region of their host galaxies. Black holes at the centers of galaxies become active when there is a large influx of gas onto the black hole that could arise from recent star formation, major mergers (Sanders et al. 1988; Barnes & Hernquist 1991; Hopkins et al. 2006)., minor mergers or recycled stellar material (Simkin et al. 1980; Genzel et al. 2008 ; Goulding et al, 2013; Rumbaugh et al, 2012). When there is no more gas to accrete, the black hole returns to its dormant state. Thus, it is theorized that AGN are just a phase of evolution that every galaxy endures.

When matter and gas accretes onto the black hole an enveloping accretion disk is formed where baryons are heated up to high temperatures and X-ray photons are released as a result of the scattering particles. Hence AGN are point like and are extremely luminous in X-ray. Because of these accretion disks, AGN are some of the most energetic objects in the universe, emitting a large amount of electromagnetic radiation on the order of $10^{41} - 10^{46}$ ergs/sec over the entire spectrum.

Any mechanism that adds to the inflow of cold gas into a galaxy has the potential to ignite star formation as well as AGN activity if cold gas can be transported to the core. Thus, the presence of AGN is linked to star formation in a galaxy (Terlevich et al. 1990; Kauffmann et al. 2003; Butcher and Oemler, 1978,1984; Martini et al, 2009; Rumbaugh et al, 2012; Goulding et al, 2014). Interestingly enough, AGN accretion and feedback are thought to regulate this galactic star formation (Silk and Reese, 1998; Di Matteo, Springel, and Hernquist, 2005; Hopkins et al, 2005; Cimatti et al, 2013; Rosario et al, 2013), stripping the galaxy of the conditions necessary for stellar nurseries to form. A galaxy's central black hole serves as a type of on and off switch such that when activated, it can be a large driver of a galaxy going from actively forming stars to being quiescent (Rumbaugh et al, 2012; Rosario et al, 2013). In support of this theory, recent studies have shown that AGN are most present in green valley galaxies, which are galaxies undergoing a transition from being a blue cloud star forming galaxy to a red sequence, elliptical galaxy (Rumbaugh et al, 2012; Cimatti et al, 2013).

Galaxies in clusters are known to evolve at different rates than galaxies in the field as the galaxy populations are observed to be different. Mechanisms for driving this different evolution include major mergers which are more prominent in galaxy groups, (Richstone 1976; Moore et al 1996), ram-pressure stripping (Gunn & Gott 1972), tidal effects, and evaporation by the hot intracluster and interstellar medium that hinders the availability and transport of cold gas to the galaxy (Cowie

and Songaila, 1977; Farouki & Shapiro 1981; Merritt 1983). By extension, the lack of cold gas available to the galaxy affects AGN activity and evolution. Because AGN activity is driven by the renewal of cold gas near the central region of its host galaxy, any mechanism responsible for the transport of matter can ignite an AGN from a previously quiescent galaxy (Martini et al, 2009, 2013). Hence, AGN activity can be inferred to be heavily dependent on its environment and it is especially useful to study AGN in different structures such a galaxy groups and clusters as well as in the field (Arnold et al, 2009).

Galaxy groups have fewer galaxies than clusters, however, their smaller gravitational potential wells allow their galaxy members to have smaller velocities and thus they are more likely to collide with one another, which could ignite AGN through major mergers (Shen et al, 2006; Sivakoff et al, 2008). In contrast, galaxies in dense cluster environments have velocity dispersions which are too high to allow bound pairs (Ghigna et al, 1998). This, combined with the larger effects of cluster processes for higher mass clusters, implies that the AGN fraction should be lower in clusters compared to galaxy groups. In support of this theory, scientists have recently shown that the AGN fraction in galaxy groups and/or the field have a higher AGN fraction than clusters (Sivakoff et al, 2008; Arnold et al, 2009; Martini et al, 2013; Oh et al, 2014).

Studies have shown that the cluster AGN fraction is observed to be the same as the field AGN fraction at higher redshift (Eastman et al, 2007; Martini et al, 2009; Martini et al, 2013). At lower redshift, the AGN fraction in clusters is lower (Martini et al, 2013). Therefore, the cluster AGN fraction evolves more strongly leading to parity with field AGN at high redshift. It follows that a positive correlation between cluster AGN and redshift is observed The implications for this would be that the conditions for igniting AGN were more favorable in the past, when a larger amount of cold gas was available compared to the present because the majority of the galaxies were still young and active with star formation (Giovanelli and Haynes, 1985). In support of this theory, scientists have observed a similar evolution in star forming cluster galaxies (e.g., Boyle et al. 1998; Franceschini et al. 1999; Butcher and Oemler, 1978,1984; Merloni et al. 2004; Haines et al, 2009; Martini et al 2009; Rumbaugh et al, 2012).

In order to effectively probe the AGN fraction in a cluster or galaxy group environment, we need X-ray properties of the cluster AGN as well as the optical properties of that AGN's host galaxy. The Dark Energy Survey is a new large optical survey intended to constrain the dark energy density by observing the growth of large scale structure and supernovae. DES has created a redMaPPer catalogue of galaxy cluster and group members (Rykoff et al, 2014). The catalogue contains galaxy cluster and group members from the science verification data from DES and provides optical properties for each galaxy such as redshift, host cluster richness (proxy for cluster mass), and magnitude.

In this paper we investigate the AGN fraction in clusters as a function of redshift and richness to probe a cluster AGN's dependence on environment and evolution from the present to z=1. We cross-match the AGN detected in Chandra Observations to the cluster galaxies detected in DES science verification redmaPPer cluster member catalogues versions 6.1.3 and 6.2.12 to obtain our sample of AGN in clusters. We calculate the X-ray counts, flux, and luminosity of the detected

point sources and then observe the AGN fraction as a function of redshift and richness with the luminosity threshold of 10^{43} ergs/sec and trend specific redshift and richness cuts.

2 Calculating the Energy Flux of AGN

If we have a point source AGN with a measured number of counts N_{source} in a particular region, those counts will be a superposition of the number of counts of the source plus the number of counts of the background noise. To get the counts registered by just the point source N_{adj}, we started off by subtracting from N_{source} in each source region the number of counts N_{ann} in a local annulus region, which is normalized to the area of the source region:

$$N_{norm} = N_{ann} \cdot \frac{A_{source}}{A_{ann}}$$

The annulus is centered at the coordinates of the detected AGN and has an inner radius equal to the radius of the source region, and an outer radius equal to twice the inner radii, unless there is a point source or cluster core in the near vicinity, in which case the outer radii is adjusted accordingly. By doing this, we obtain the raw number of counts due to the source N_{adj}:

$$N_{adj} = N_{source} - N_{norm}$$

The purpose of this is eliminate the background counts registered in the source region which is attributed to local noise. The error in the number of registered counts follows a poisson distribution, hence:

$$\sigma_{N_{source}} = \sqrt{N_{source}}$$

$$\sigma_{N_{ann}} = \sqrt{N_{ann}}$$

$$\sigma^2_{N_{norm}} = \left(\frac{A_{source}}{A_{ann}}\right)^2 \cdot N_{ann}.$$

Furthermore, by derivative propagation of error:

$$\left(\sigma_{N_{adj}}\right)^2 = N_{source} - \left(\left(\frac{A_{source}}{A_{ann}}\right)^2 \cdot N_{ann}\right)$$

The photon flux F_{photon} is obtained by dividing the adjusted counts of a source by the observation's average exposure over the source area:

$$F_{photon}\left(\frac{photons}{cm^2 \cdot sec}\right) = \frac{N_{adj}\ (photons)}{exposure\ (cm^2 \cdot sec)}$$

The complimentary propagated error is

$$\sigma^2_{F_{photon}} = \left(\frac{1}{exposure}\right)^2 \cdot \sigma^2_{N_{adj}}$$

To calculate the energy flux, the photon flux for a given energy E is measured with a $\Gamma = 1.7$ power law model such that

$$\frac{dF_{photon}}{dE} = AE^{-1.7}$$

Where A is a normalization constant. Multiplying by dE and integrating we have

$$\int dF_{photon} = \int_{E_1}^{E_2} AE^{-1.7} dE$$

E_1 and E_2 are the energy bounds of the Chandra observations, 0.3 keV and 7.9 keV respectively. Furthermore, multiplying both sides by the energy E gives us the relation for the energy flux of an AGN:

$$F_E = \int_{E_1}^{E_2} A \cdot E \cdot E^{-1.7} dE = \int_{E_1}^{E_2} AE^{-0.7} dE$$

We are able to solve for the energy flux without knowing the normalization constant A by dividing the energy flux by the photon flux such that

$$\frac{F_E}{F_{photon}} = \frac{\int_{E_1}^{E_2} AE^{-0.7} dE}{\int_{E_1}^{E_2} AE^{-1.7} dE} = \frac{\left(-\frac{1}{0.7}\right) \cdot (E_2^{-0.7} - E_1^{-0.7})}{\left(\frac{1}{0.3}\right) \cdot (E_2^{0.3} - E_1^{0.3})} = R$$

Thus it follows that

$$F_E = F_{photon} \cdot R$$

and

$$\sigma_{F_E}^2 = \left(\sigma_{F_{photon}}\right)^2 \cdot R^2$$

where $R = 2.0813 \cdot 10^{-9}$.

3 Cluster AGN Selection

We use wavdetect, a wavelet source detection tool available in CIAO which accounts for the point spread function of off axis AGN, to determine the number of point sources in a the energy range 0.3-7.9 keV in 93 distinct Chandra observations (the complete list is stated in the appendix). We calculate the X-ray flux and luminosity of each source assuming a power law of $\Gamma = 1.7$, as described in the previous section. We use circular regions ranging from 5-25 arc seconds that envelope the source to calculate the photon flux, and annulus regions with inner radii ranging from 10-20 arc seconds and outer radii ranging from 20-40 arc seconds are centered at the point source and used to calculate the background error on the number of counts. We calculate the number of photon counts in each region with the imaging software ds9 and CIAO tools (Fruscione et al. 2006).

To obtain our sample of AGN in clusters we match the positions of detected cluster galaxies from the DES redMaPPer galaxy member catalogue v. 6.2.12 to the point sources detected by Chandra to within 2 arc seconds. Cluster AGN identified in both Chandra and DES now have associated X-ray luminosities as well as optical properties of their host galaxies such as redshift, magnitude, and cluster identification number.

Each cluster galaxy is assigned a probability of being part of an individual cluster. The sum of the probabilities of each galaxy thought to be in a given cluster is defined as that cluster's richness (λ) Hence, a clusters richness is to a good approximation, the number of galaxies that a cluster has, and is a quantity which correlates with cluster mass. DES has a separate redMaPPer cluster catalogue v. 6.2.12 which tabulates the richness of each cluster.

Because of the large amount of thermal bremsstrahlung emitted from cluster cores in our X-ray observations, wavdetect often mistakenly identified the core of a cluster as a point source. We manually check each point source with ds9 and eliminate any large diffuse sources larger than 25 arc seconds in radius which can be attributed to cluster core emission. Similarly, cluster AGN are often found near the cluster core. Noise in the background of the point source attributed to bremsstrahlung can be too large compared to the signal of the AGN, which thus alters the statistics negatively. Such AGN are eliminated from our sample.

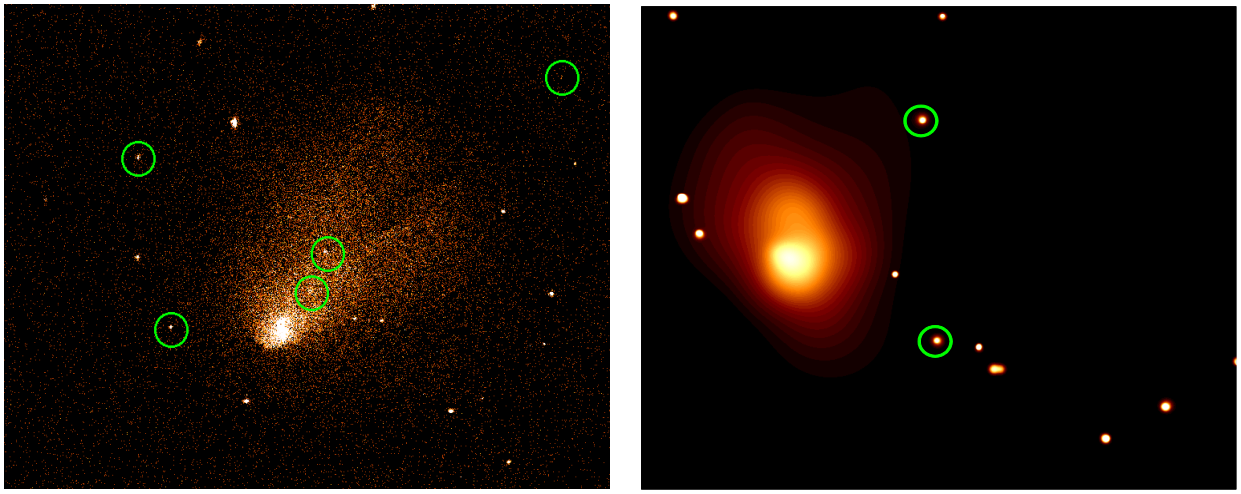

Figure 1. Left: The central region of the El Gordo cluster has more diffuse X-ray emission than that of point sources, which are highlighted in green. Wavdetect often mistakes the diffuse emission of a cluster core for a point source with a large point spread function, and thus we must eliminate these cluster cores from our sample. Right: A smoothed Chandra image of the Cluster SPT-CLJ0449-4901 with two cluster AGN highlighted with green circles. The cluster core is the larger more diffuse X-ray emission present in the image. Smoothed images are used to determine if a questionable source is really point-like compared to the surrounding regions

For AGN that have a low amount of counts or do not look point-like in nature, we refer to smoothed Chandra images such as in Figure 1 which are good indications of whether sources are point like relative to their surrounding regions.

Once AGN are cross matched with their host galaxies, we use the redshifts of the host galaxies from the redmaPPer catalogues to calculate luminosity distance d_L. We do so by using Ned Wright's (2006) cosmological calculator for luminosity distance using assuming a ΛCDM universe where Ω_{vac}=0.714, Ω_M=0.286 and H_o=69.6. We then calculate the X-ray luminosity:

$$F_E = \frac{L}{4\pi {d_L}^2}$$

Solving for L we now have

$$L = F_E \cdot 4\pi d^2$$

The complimentary error for the luminosity is then

$$\sigma_L^2 = \left(\sigma_{F_E}\right)^2 \cdot (4\pi d^2)^2$$

4 Final Cluster AGN Sample for Redshifts 0<z<1

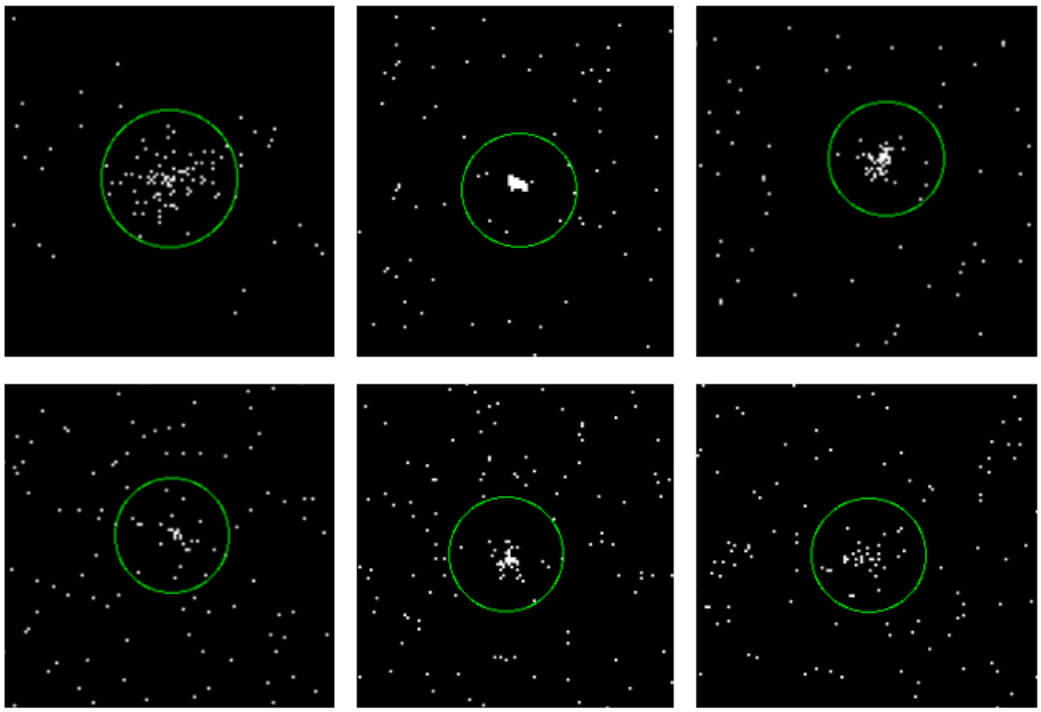

Figure 2. Above are six of the 149 point sources we detected in Chandra that have matching host galaxies in clusters from DES. The green circles are the regions used to calculate the number of counts for each source.

The complete set of detected cluster AGN is shown in the appendix. We accumulated a sample of 149 AGN identified in clusters, with most clusters having richness between 5-150, and a few having richness above 150, such as Abell S1063 and the El Gordo cluster. Some examples of detected cluster AGN in our sample are shown in Figure 2 above. To have the most complete AGN fraction, we probed Chandra for which clusters fell within our Chandra observations, and accumulated a total of 669 clusters with and without AGN detected in Chandra observations overlapping with DES observation data

The AGN fraction is measured as the number of cluster AGN over the sum of the richnesses of clusters detected in a given richness or redshift bin. The error follows a poisson distribution, and is calculated as $\sqrt{\sum AGN} \,/\, \sum clusters$ for a given bin.

We investigate the AGN fraction as both a function of richness and redshift with several cuts to our data that are described in detail in the next section.

5 Luminosity, Richness and Redshift Cuts

Observations with a deeper field or longer exposure time are more likely to detect low flux AGN which could be AGN of low luminosity or at high redshift. Typically, only high luminosity objects are detected for large redshifts, which skews the amount of AGN detected in clusters at those redshifts. As one can see in Figure 3, AGN luminosity as a function of redshift clearly has a positive trend. As shown for reference in Figure 3, we make one luminosity cut to our data to avoid this type of bias at $L = 10^{43}\,\frac{ergs}{sec}$ (dashed line).

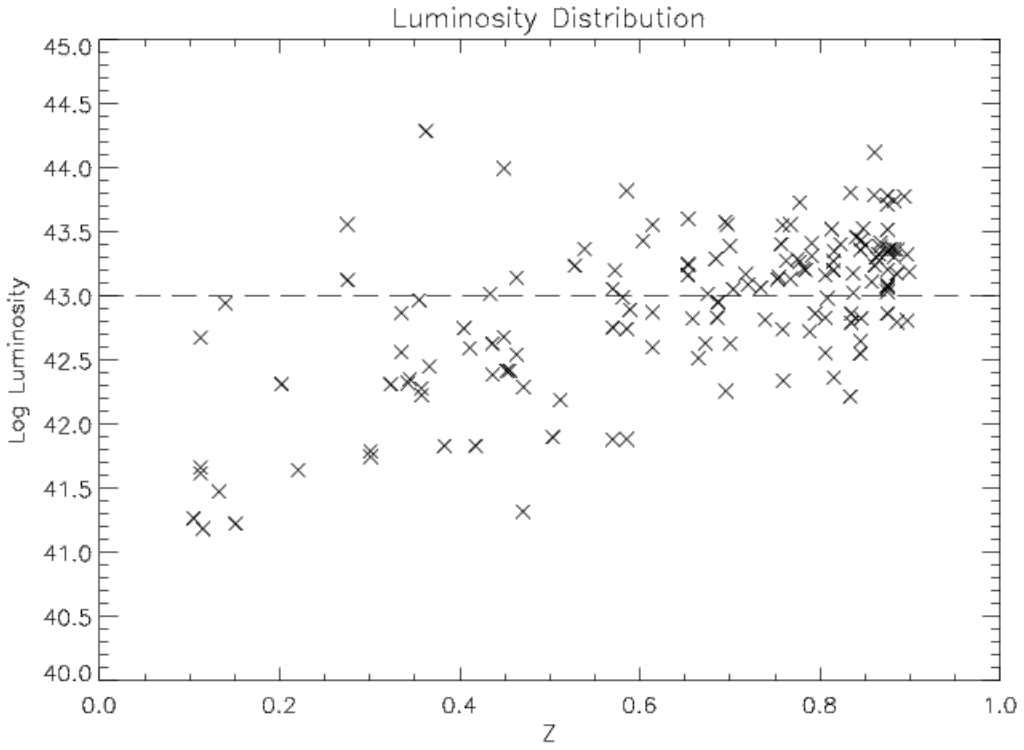

Figure 3. The distribution of luminosities as a function of redshift for our cluster AGN. The dashed line represents the luminosity cut of the data at $L=10^{43}$ ergs/sec.

When observing the cluster AGN fraction as a function of redshift we want to eliminate any bias that the AGN fraction has due to dependence on cluster mass. Similarly, when we document the AGN fraction as a function of richness, we want to avoid any bias being contributed to the AGN fraction's dependence on redshift. Hence, in addition to our luminosity cut, we present some of our data with additional redshift and richness cuts to prevent biases that may occur when observing the AGN fraction as a function of either redshift or richness.

6 AGN Fraction as a function of Redshift

In this section we present three trends of the AGN fraction as a function of redshift, all of the trends will have a luminosity threshold $L>10^{43}$ ergs/sec, one of the trends will have an additional richness cut of $\lambda>25$, and one of the trends will have a richness cut of $5<\lambda<25$. The results are summarized in Table 1.

Table 1

λ Cut	Redshift bin	AGN detected	Clusters Sampled	Σλ	AGN Fraction	σ_F
none	0.2<z<0.4	3	85	1615.8	0.00186	0.00107
	0.4<z<0.6	8	155	2117.46	0.00378	0.00134
	0.6<z<0.8	31	189	2134.74	0.0145	0.00261
	0.8<z<1	40	230	2452.89	0.0163	0.00258
λ<25	0.2<z<0.4	1	69	650.351	0.00154	0.00154
	0.4<z<0.6	5	139	1336.52	0.00374	0.00167
	0.6<z<0.8	27	179	1617.42	0.0167	0.00321
	0.8<z<1	29	224	1979.7	0.0146	0.00272
λ>25	0.2<z<0.4	2	16	965.448	0.00207	0.00146
	0.4<z<0.6	3	16	780.939	0.00384	0.00222
	0.6<z<0.8	4	10	517.323	0.00773	0.00387
	0.8<z<1	11	6	473.189	0.0232	0.00701

Table 1. The number of AGN and clusters detected for each redshift bin and richness cut, along with the richness sum of the clusters detected in each bin, the AGN fraction and the fraction error $\sigma_{F.}$ The luminosity threshold for this sample is 10^{43} ergs/sec.

To investigate the trend between the number of cluster AGN as a function of redshift, we separate our cluster AGN into four equal redshift bins, from $0.2<z<1$ (Refer to table 1). Note that the redshift bin $0<z<0.2$ is not being used, because that region held an insufficient amount of clusters that led to a relatively large statistical error in comparison to the other redshift bins. For AGN with $L>10^{43}$ ergs/sec with no richness threshold we observe the AGN fraction to increase by a factor of approximately 8.8 (refer to Figure 4). The high redshift AGN fraction is greater than the low redshift AGN fraction at 5σ. This trend is consistent with Martini et al's (2009) findings that the AGN fraction increases by factor of eight from the present to $z\sim1$. However, we must use caution when comparing data due to the fact that Martini et al's definition of AGN fraction differs slightly from our own, for example, an additional magnitude threshold is applied to all cluster galaxies detected, which is a cut that we did not take into account with our sample.

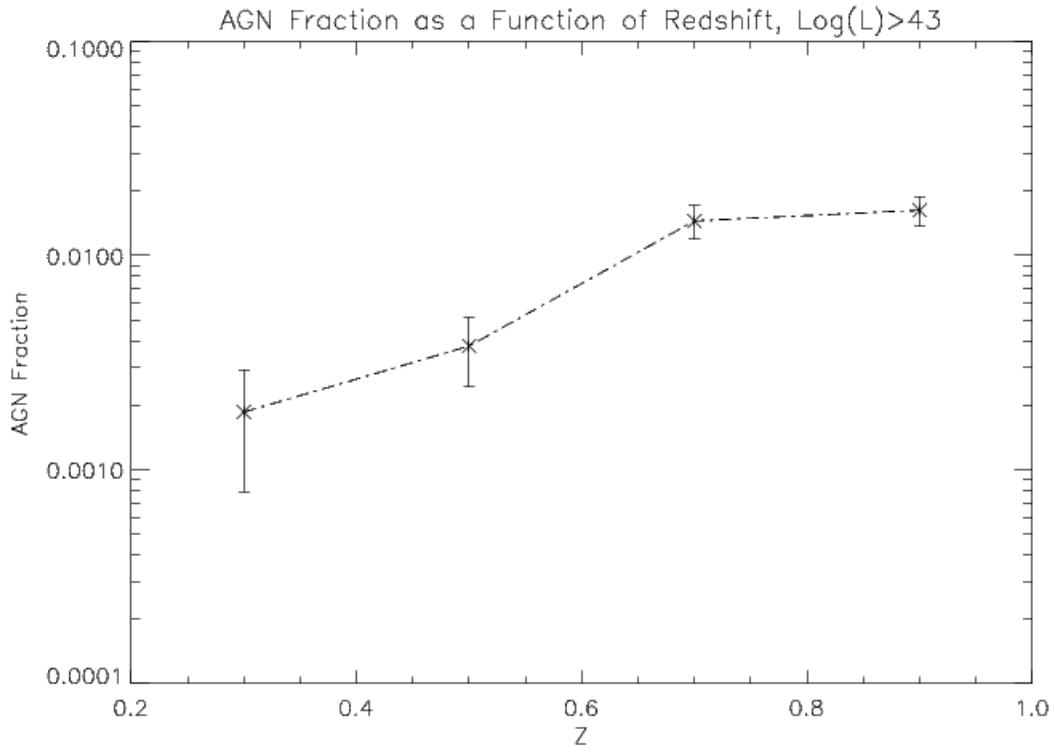

Figure 4. The AGN fraction as a function of redshift for four equally spaced redshift bins between 0.2 and 1. No cuts based on cluster richness were applied.

Next, we observed the AGN fraction for galaxy groups with a richness of less than 25 (see Figure 5). We observe the AGN fraction to increase by a factor of 9.5. The high redshift AGN fraction is greater than the low redshift AGN fraction at 4σ. Finally, we make a richness cut of $\lambda>25$, which excludes galaxy groups and only sheds light on the evolution of AGN in more massive clusters (See Figure 6). We observe the AGN fraction increase by over a factor of 11.2. Furthermore the high redshift AGN fraction is greater than the low redshift AGN fraction at 2σ. Interestingly, the AGN fraction is slightly lower yet comparable in groups than in clusters, and similarly the AGN in lower mass galaxy groups appear to evolve at a comparable rate as those in higher mass clusters.

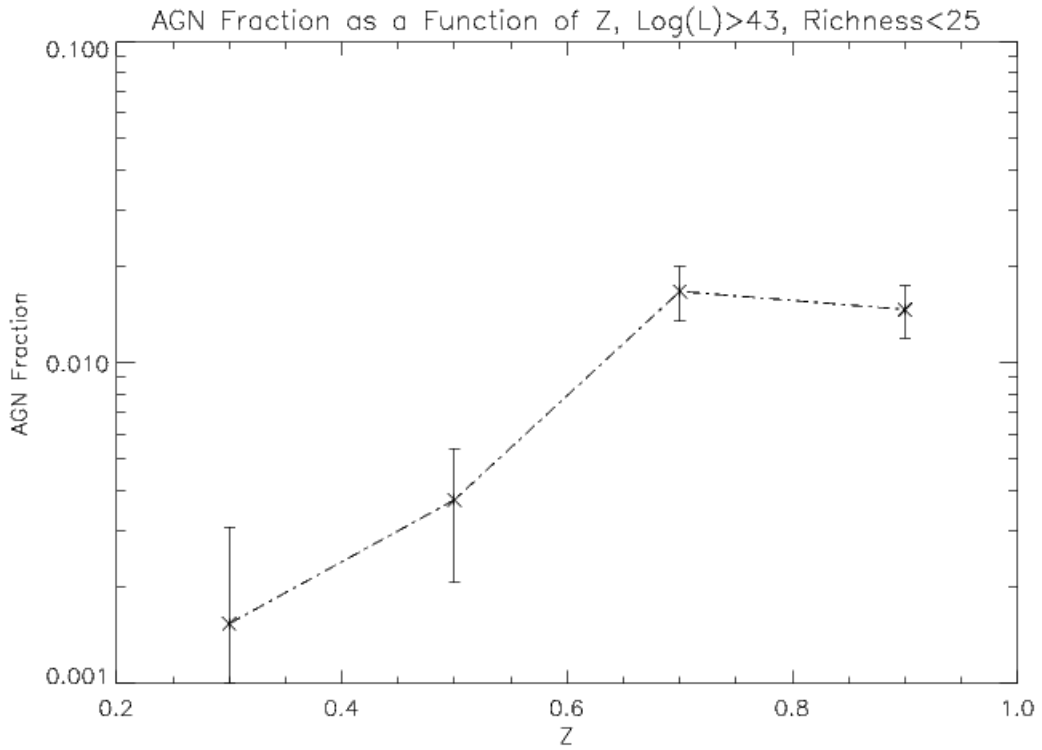

Figure 5. The AGN fraction as a function of redshift for four equally spaced redshift bins between 0.2 and 1. A richness cutoff λ<25is applied to the sample.

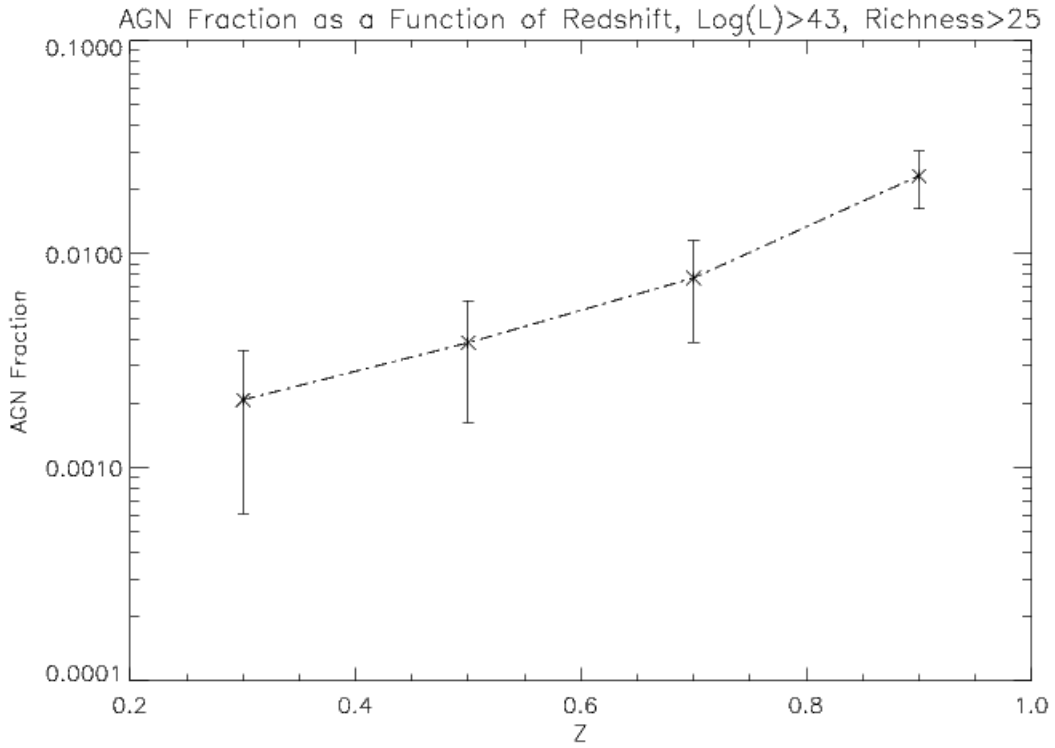

Figure 6. The AGN fraction as a function of redshift for four equally spaced redshift bins between 0.2 and 1. A richness cutoff λ>25 is applied to the sample.

7 AGN Fraction as a function of Richness

In this section we present two trends of the AGN fraction as a function of richness (see Figure 7), both of the trends will have luminosity cuts of $L>10^{43}$ ergs/sec and either a redshift cut of $0.2<z<0.6$ or a redshift cut of $0.6<z<1$.

Table 2

Z Cut	Richness Bins	AGN detected	Clusters Sampled	Σλ	AGN Fraction	σ_F
0.2-0.6	5-25	6	208	1986.88	0.00302	0.00123
	25-50	2	22	734.742	0.00272	0.00192
	50-200	3	10	1011.65	0.00297	0.00171
0.6-1	5-25	56	403	3597.11	0.0156	0.00208
	25-50	2	7	235.490	0.00849	0.00601
	50-200	13	9	755.022	0.0172	0.00478

Table 2. The number of AGN and clusters detected for each richness bin and redshift cut, along with the richness sum of the clusters detected in each bin, the AGN fraction and the fraction error σ_F. The luminosity threshold for this sample is 10^{43} ergs/sec.

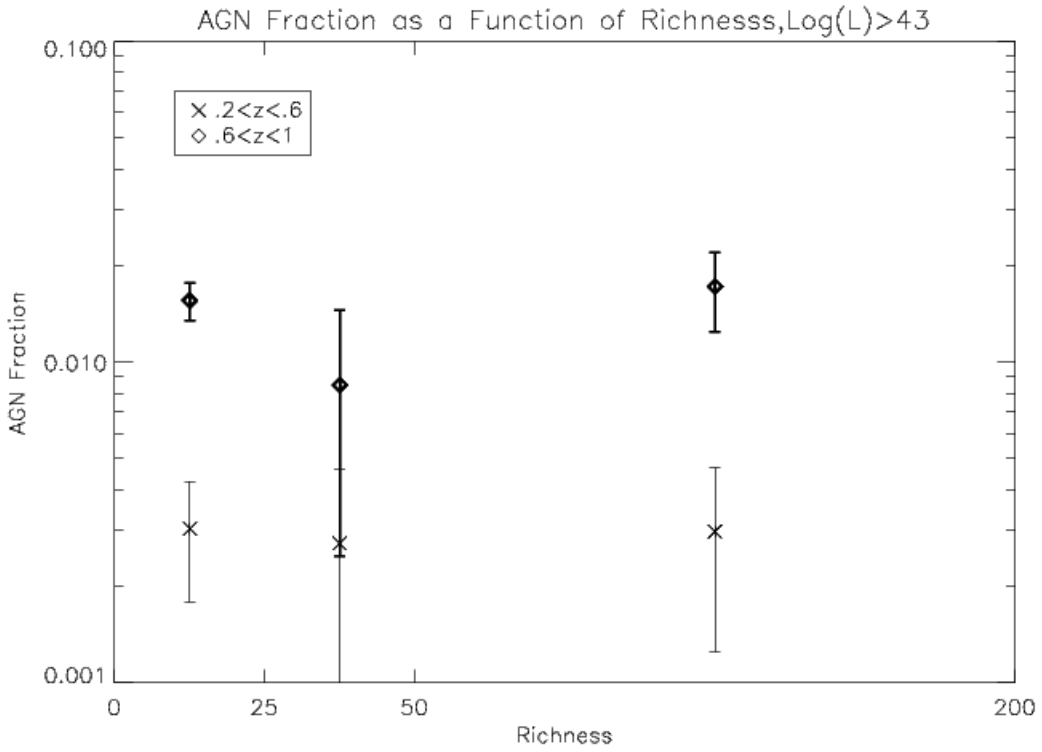

Figure 7. The AGN fraction as a function of richness for three bins of low, intermediate and high richness for two redshift cuts of $0.2<z<.6$ and $0.6<z<1$.

To observe the trend between the AGN fraction and environment, we choose 3 bins of richnesses, which are $5<\lambda<25$ (low richness), $25<\lambda<50$ (intermediate richness), and $50<\lambda<200$ (high richness) for two separate redshift bins of $0.2<z<0.6$ and $0.6<z<1$. The redshift cuts are created so that the trend between AGN and redshift is approximately accounted for in our plot and does not bias any AGN dependence on richness. For both the high and low redshift limited sample the AGN fraction has no significant trend with cluster richness. Thus our data infers that there is no significant AGN fraction increase or decrease between cluster groups and massive clusters. A larger sample of intermediate to high richness clusters for both high and low redshifts would shed light on if a trend actually exists between these different environments.

8 Discussion and Conclusions

From the analysis, we can definitely conclude that with our current definition of the AGN fraction there is a mild positive trend between the AGN fraction and redshift, reaffirming the theory that AGN in dense environments where more frequent at earlier times in the universe. For AGN in clusters of all richnesses the AGN fraction increases from redshift 0.2 to 1 by a factor of 8.8 where the high redshift AGN fraction is greater than the low redshift AGN fraction at 5σ. If the sample is cut into AGN in low richness clusters and high richness clusters, the AGN fraction increases from $0.2<z<1$ by a factor of 9.5 and 11.2 where the high redshift AGN fraction is greater than the low redshift AGN fraction at 4σ and 2σ respectively. The AGN fraction in each redshift bin is comparable for both richness cuts, which implies that the fraction of galaxies hosting AGN in a structure is not heavily dependent on the environment. This is supported by our analysis of the AGN fraction as a function of cluster richness, which does not show a strong definite trend for either low or high redshift cuts.

The similar evolution of the AGN fraction as a function of redshift for low and high richness cuts implies that different physical processes characteristic to either galaxy groups or clusters that are responsible for the quenching or surplus of cold gas have approximately the same effect on how AGN evolve in these different environments. In addition, the comparable AGN fraction from low to high richness clusters implies that conditions in the cluster environment that are favorable to ignite AGN are present in both high and low mass clusters.

For galaxy groups, because they are less gravitationally bound systems, the average velocity dispersion of galaxy members is lower and hence galaxies are more likely to interact and form major mergers which are thought to be a mechanism responsible for igniting high luminosity AGN, . For larger clusters the high velocity dispersion of galaxy members makes it difficult for major mergers to develop. Hence one would expect that if major mergers were the primary mechanisms in igniting AGN, the AGN fraction would be higher in groups than it is in clusters. Since we observe that the AGN fraction is about the same for both groups and clusters, we can infer that galaxy mergers likely do not play major roles in AGN ignition.

We theorize that the AGN fraction as a function of redshift is positive primarily because there was more cold gas that was available to accrete onto the central SMBH in cluster members at high redshift compared to the present. Gravitationally bound systems at high redshift had a larger fraction of younger, bluer galaxies with active star formation (Butcher and Oemler, 1978, 1984),

whose dense molecular clouds and recycled stellar material from supernova explosions ignited a larger fraction of AGN in the cluster environment.

Processes such as ICM heating and ram-pressure stripping are thought to be the mechanisms for affecting the availability of cold gas to fuel the AGN. These processes are dependent on the potential well of the system, and thus would be weaker for groups than in clusters, which could be an explanation for the slightly lower rate of evolution of AGN for groups. However, if there is indeed more cold gas available to structures at earlier times in the universe, one might expect that feedback from AGN could possibly be more frequent, which could speed up AGN evolution and quenching of material even when the effects caused by the structure are weak. This could be a partial explanation for why the AGN fraction evolves at a comparable rate for both low and high richnesses.

9 Future Work

The next step in our analysis is to recreate our cluster AGN sample with the most recent and final version of the redMaPPer catalogue from DES science verification data. Furthermore, we wish to redefine the AGN fraction such that it is a more accurate and unbiased representation of how many AGN there are in the cluster galaxies within Chandra and DES observations. Because cluster AGN are dependent on the galaxy members detected in the DES redMaPPer catalogue, we need to interpret the probability that these galaxies are members of clusters as the number of AGN detected. Then, the AGN fraction would be modified to become the number of AGN detected over the actual number of galaxies in clusters detected in both DES and Chandra. To effectively do this we must also carefully determine which individual cluster galaxies physically fall within the Chandra observations. In the future, when the year one data from the Dark Energy Survey becomes available to us, we will be able to accumulate an even larger sample of cluster AGN for our analysis.

In order to truly understand why the AGN fraction does not change significantly or evolve differently from groups to clusters, we need to obtain a better understanding of the processes that govern the triggering and shutting off of AGN in different environments. In relation to this, we could document the color magnitude of each cluster galaxy that hosts an AGN to see if AGN are more prominent in blue cloud, red sequence, or green valley galaxies. Another environmental factor we could probe is a cluster AGN's distance from the cluster core, which would reveal more about the environmental effects that cluster processes has on AGN frequency.

10 References

Arnold, T. J.,Martini, P.,Mulchaey, J. S., Berti, A.,&Jeltema, T. E. 2009, ApJ, 707, 1691

Barnes, J. E., & Hernquist, L. E. 1991, ApJL, 370, L65

Boyle, B. J., Georgantopoulos, I., Blair, A. J., et al. 1998, MNRAS, 296, 1

Butcher, H., & Oemler, A. 1978, ApJ, 219, 18

Butcher, H., & Oemler, A. 1984, ApJ, 285, 426

Cimatti, A., Brusa, M., Talia, M., et al 2013, APJ, 1, 1311

Cowie, L. L., & Songaila, A. 1977, Natur, 266, 501

Di Matteo, T., Springel, V., & Hernquist, L. 2005, Nature, 433, 604

Eastman, J.,Martini, P., Sivakoff, G., et al. 2007, ApJ, 664, L9

Farouki, R., & Shapiro, S. L. 1981, ApJ, 243, 32

Ferrarese, L., &Merritt, D. 2000, ApJL, 539, L9

Ford, H. C., Tsvetanov, Z. I., Ferrarese, L., et al 1998, IAUS, 184, 377F

Franceschini, A., Hasinger, G., Miyaji, T., & Malquori, D. 1999, MNRAS, 310, L5

Fruscione et al. 2006, SPIE Proc. 6270, 62701V, D.R. Silvia & R.E. Doxsey, eds

Gebhardt, K., Bender, R., Bower, G., et al. 2000, ApJL, 539, L13

Genzel, R., Burkert, A., Bouch´e, N., et al. 2008, ApJ, 687, 59

Ghigna, S., Moore, B., Governato, F., Lake, G., Quinn, T., & Stadel, J. 1998, MNRAS, 300, 146

Giovanelli, R., & Haynes, M. P. 1985, ApJ, 292, 404

Goulding, A. D., Forman, W. R., Hickox, R. C. et al 2014, APJ, 783, 40

Graham, A. W. 2015, in Galactic Bulges, ed. E. Laurikainen, R. F. Peletier, & D. Gadotti (Berlin: Springer), in press (arXiv:1501.02937)

Gunn, J. E., & Gott, J. R. I. 1972, ApJ, 176, 1

Haehnelt, M. G., Kauffmann, G. 2000, Astron. Soc. 318, 35

Haines, C. P., Smith, G. P., Egami, E., et al. 2009, ApJ, 704, 126

Hopkins, P. F., et al. 2005, ApJ, 630, 705

Hopkins, P. F., Hernquist, L., Cox, T. J., et al. 2006, ApJS, 163, 1

Kauffmann, G., Heckman, T. M., Tremonti, C., et al. 2003, MNRAS, 346, 1055

Martini, P., Miller, E. D., Brodwin, M. et al 2013, ApJ, 768, 1

Martini, P., Sivakoff, G. R., & Mulchaey, J. S. 2009, ApJ, 701, 66

Merloni, A., Rudnick, G., & DiMatteo, T. 2004, MNRAS, 354, L37

Merritt, D. 1983, ApJ, 264, 24

Moore, B., Katz, N., Lake, G., Dressler, A., & Oemler, A., Jr. 1996, Natur, 379, 613

Oh, S., Mulchaey, J. S., Woo, J. H. et al 2014, ApJ, 790, 43

Planelles, S., Schleicher, D.R.G., Bykov, A. M. 2014, APJ, 1404, 3956

Richstone, D. O. 1976, ApJ, 204, 642

Rosario, D.J., Mozena, M., Wuyts, S., et al 2013, APJ, 763, 59

Rumbaugh, N., Kocevski, D. D., Gal, R. R., et al. 2012, ApJ, 746, 155

Rykoff E. S. et al., 2014, ApJ, 785, 104

Sanders, D. B., Soifer, B. T., Elias, J. H., et al. 1988, ApJ, 325, 74

Silk, J., & Rees, M. J. 1998, A&A, 331, L1

Simkin, S.M., Su, H. J., & Schwarz,M. P. 1980, ApJ, 237, 404

Sivakoff, G. R., Martini, P., Zabludoff, A. I., Kelson, D. D., & Mulchaey, J. S. 2008, ApJ, 682, 803

Shen, Y., et al. 2006, ApJ, 654, L115

Tremaine, S., Gebhardt, K., Bender, R., et al. 2002, ApJ, 574, 740

Terlevich, E., Diaz, A. I., & Terlevich, R. 1990, MNRAS, 242, 271

Xu, B. X., Wu, X. B., Zhao, H. S. 2007, APJ, 664, 198

Wright E. L., 2006, PASP, 118, 1711

11 Appendix

Table 3 tabulates the X-ray and optical properties of the detected cluster AGN and its host cluster in Chandra and DES. The properties listed include: the position of each point source, the X-ray luminosity, cluster ID from the redMaPPer v 6.2.5 catologue of each AGN's host cluster, the observation ID of the Chandra observation that the AGN was detected in, the cluster redshift which to a good approximation is the redshift of the host galaxy and AGN, and the cluster richness. There are 149 total AGN in this current analysis.

Table 3.

RA	DEC	X-Ray Luminosity (ergs/sec)	Cluster ID	Obs. ID	Cluster Z	Cluster Richness
55.104940	-28.6775	1.84626E+41	38	9385	0.104246	44.5335
65.547279	-50.1419	4.72458E+42	8720	11866	0.11218	8.13511
65.618837	-50.1492	4.57993E+41	8720	11866	0.11218	8.13511
65.642096	-50.0903	4.16956E+41	8720	11866	0.11218	8.13511
149.47888	2.52185	1.53083E+41	15943	15259	0.11475	6.25875
150.41570	2.43021	2.98034E+41	1646	7995	0.132357	13.3371
73.887451	-51.2599	2.08237E+41	5515	13474	0.139478	7.60119
342.30409	-44.4986	1.67343E+41	13170	4966	0.150849	5.03835
150.17321	1.61638	2.06106E+42	384	15224	0.201879	27.7072
150.0909	2.391251	4.38835E+41	321	8123	0.220464	29.2938
67.13046	-53.8017	1.3282E+43	301	6956	0.275156	35.1364
67.183314	-53.8265	3.61799E+43	301	6956	0.275156	35.1364
150.39475	2.06836	6.15092E+41	4331	8010	0.300688	10.5301
150.44735	2.05396	5.56979E+41	4331	8553	0.300688	10.5301
150.18003	1.76890	2.04932E+42	4029	15224	0.32306	13.7642
78.981230	-54.4377	7.40303E+42	6	15099	0.335036	8.37919
78.932700	-54.4943	3.63609E+42	6	15099	0.335036	8.37919
149.89899	2.46672	2.09715E+42	13931	8004	0.342351	8.18088
72.302783	-49.0881	1.64595E+42	18968	13473	0.344352	6.22824
65.594894	-50.1761	9.29481E+42	10189	11866	0.354981	9.67587
70.621076	-48.9425	1.91125E+42	13512	13475	0.357297	7.12829
150.08298	2.30485	1.68333E+42	10228	8007	0.357783	7.90629

149.70072	2.40267	1.92707E+44	10015	8008	0.36219	8.73006
342.13521	-44.4510	2.81762E+42	3	4966	0.366181	185.123
15.530036	-49.2998	6.78997E+41	22690	14022	0.382625	7.08252
8.9247500	-43.2837	5.60138E+42	19142	7016	0.404668	7.4639
73.78532	-53.4045	3.93053E+42	280	3930	0.410998	40.2163
73.602657	-53.4183	6.80147E+41	11774	3930	0.417421	8.80633
65.07277	-50.5318	1.04228E+43	2584	5541	0.433682	24.0155
150.19204	1.57778	4.26051E+42	8398	15224	0.436102	11.5217
150.51153	2.10953	2.42844E+42	3003	8005	0.436351	22.8104
73.589265	-53.2587	4.7742E+42	4381	3930	0.448712	16.327
78.850016	-54.5831	9.88313E+43	6789	15099	0.448955	11.2471
66.593478	-54.8848	2.61024E+42	19880	13472	0.45193	5.72483
150.66045	2.26548	2.62575E+42	20310	15230	0.455275	9.49281
77.354821	-53.7167	3.48304E+42	258	9432	0.462841	56.7832
77.375264	-53.6786	1.38901E+43	258	9432	0.462841	56.7832
74.128677	-51.1849	2.30879E+42	20340	13474	0.4701	7.28084
55.140122	-28.6784	1.95178E+42	16139	9385	0.470554	8.82159
149.77705	2.75693	7.92523E+41	1204	15213	0.503278	19.7899
150.20921	1.85429	1.54455E+42	11768	8023	0.511382	7.69272
150.00908	2.27503	1.71809E+43	31151	8497	0.527497	5.20616
64.479055	-47.9548	2.32339E+43	8187	13397	0.538514	6.48758
74.046484	-51.2857	7.58235E+41	37	13474	0.569654	88.6051
74.119554	-51.2683	2.42609E+43	37	13474	0.569654	88.6051
74.151041	-51.2298	8.78033E+42	37	13474	0.569654	88.6051
71.504224	-58.7800	1.58115E+43	3971	13482	0.572401	13.1845
71.606225	-58.6996	9.76083E+42	6473	13482	0.580651	11.9183
64.319107	-47.8583	6.62017E+43	87	13397	0.585119	67.2939
64.338490	-47.8530	5.53929E+42	87	13397	0.585119	67.2939
64.371292	-47.8935	7.63847E+41	87	13397	0.585119	67.2939

71.688997	-58.8861	7.8186E+42	5406	13482	0.588677	6.77742
64.241880	-47.8744	2.69448E+43	221	13397	0.603428	6.16722
66.47593	-54.9158	3.59372E+43	19	13472	0.613893	5.67906
66.51899	-54.9115	3.97977E+42	19	13472	0.613893	5.67906
66.543092	-54.9229	7.44519E+42	19	13472	0.613893	5.67906
150.31430	2.38164	1.45777E+43	33597	8123	0.653147	6.39605
79.111229	-54.5495	1.78802E+43	1351	15099	0.653409	23.4969
79.043739	-54.5509	4.00546E+43	1351	15099	0.653409	23.4969
79.069703	-54.5302	1.73919E+43	1351	15099	0.653409	23.4969
149.90596	2.39649	6.68855E+42	22008	8483	0.658222	6.12146
15.568012	-49.2461	3.27661E+42	11350	14022	0.664824	12.498
71.851553	-58.9019	1.88224E+43	758	15560	0.672723	33.8855
150.04032	2.47127	1.0397E+43	1866	8002	0.675098	15.549
150.18797	2.35295	1.95238E+43	32671	8002	0.68417	6.01467
149.98773	2.58530	6.81451E+42	4072	7998	0.685781	13.9015
66.689656	-54.8979	8.95897E+42	15409	13472	0.686808	10.1793
15.426716	-49.3874	3.79597E+43	5356	12258	0.694864	13.4133
150.05856	2.60210	1.81742E+42	2352	7998	0.695094	23.741
78.911674	-54.4404	3.6116E+43	26355	15099	0.696802	5.03835
15.591503	-49.3596	2.4489E+43	16164	14022	0.699901	5.28243
15.599993	-49.3756	4.26408E+42	16164	14022	0.699901	5.28243
149.92606	2.52635	1.12839E+43	84	7998	0.703567	82.2743
150.15838	1.71350	1.48431E+43	23255	15225	0.717389	7.14354
15.771757	-49.4407	1.22976E+43	13585	12258	0.720069	9.61485
79.178057	-54.5492	1.16532E+43	4269	9331	0.734141	7.06727
15.419026	-49.3240	6.55342E+42	6274	14022	0.738817	13.3371
66.802753	-54.9153	1.35341E+43	30247	13472	0.752748	6.74691
150.04871	2.32214	1.40928E+43	26150	8002	0.75433	5.72483
66.841128	-54.7700	2.54442E+43	41216	13472	0.75652	5.70957

71.541921	-58.8448	5.51622E+42	12952	13482	0.758262	8.53174
67.421090	-53.9311	3.55055E+43	39780	6956	0.758338	7.41813
73.565892	-53.2898	2.184E+42	12067	3930	0.759326	10.5454
71.693979	-58.7671	1.45061E+43	14724	15560	0.762436	17.5322
66.460270	-55.0133	3.62514E+43	8546	13472	0.767245	12.6201
66.521356	-55.0196	1.36005E+43	8546	13472	0.767245	12.6201
15.556891	-49.2833	1.93702E+43	5080	14022	0.77472	19.7747
71.65783	-48.5762	5.36068E+43	314	7802	0.777365	50.849
71.678931	-48.6007	1.85137E+43	314	7802	0.777365	50.849
342.10592	-44.6154	1.63395E+43	69246	4966	0.78135	8.19613
150.03032	2.35874	1.60079E+43	35204	8008	0.783901	6.7164
150.07476	1.65959	5.27487E+42	38682	15224	0.788478	5.57228
70.436461	-48.8419	2.04891E+43	6054	14372	0.790512	9.44704
70.456318	-48.8609	2.57345E+43	6054	14372	0.790512	9.44704
74.128982	-51.3184	1.13977E+43	7889	13474	0.794336	5.75534
72.23688	-49.0426	3.57366E+42	60	13473	0.805804	92.007
72.24063	-49.0013	6.78355E+42	60	13473	0.805804	92.007
72.257297	-48.9994	2.24018E+42	60	13473	0.805804	92.007
150.37381	2.13122	9.61421E+42	54161	8005	0.807849	5.6333
69.626321	-54.3968	3.31722E+43	19691	12259	0.812776	12.3607
150.57310	2.20353	1.8678E+43	19611	15229	0.814719	8.50123
150.53743	2.18747	1.59033E+43	19611	8000	0.814719	8.50123
74.072382	-51.1274	5.51701E+43	42308	13474	0.815033	8.44021
70.45223	-48.913	2.23073E+43	56	13475	0.815281	86.3779
71.805850	-48.5409	2.5385E+43	6438	7802	0.822531	6.35028
74.097354	-51.3445	7.31285E+42	29368	13474	0.833464	7.9368
150.504	2.224471	6.409E+43	2900	15230	0.833768	14.9388
71.562897	-58.7240	6.19875E+42	56782	13482	0.834484	5.20616
15.783317	-49.3710	7.28475E+42	66587	12258	0.834548	5.48075

70.508262	-49.0086	1.50637E+43	37644	13475	0.836513	6.7164
150.18144	2.42345	1.05652E+43	49678	8123	0.836585	5.61804
150.42721	2.08309	2.87729E+43	10610	15228	0.840357	9.99622
149.56947	2.41867	4.45657E+42	8594	15242	0.844534	16.4033
149.53328	2.45829	3.55216E+42	8594	15242	0.844534	16.4033
150.16083	2.33259	2.28633E+43	44124	8007	0.844807	5.17565
150.54183	2.15431	6.69484E+42	21610	15230	0.845491	7.17405
150.54035	2.16791	2.72073E+43	21610	15230	0.845491	7.17405
69.328370	-54.3552	3.36859E+43	21109	12259	0.847975	11.476
342.21138	-44.5660	2.45846E+43	31298	4966	0.850155	8.2419
342.29236	-44.3944	1.29275E+43	17066	4966	0.857252	10.9573
66.654772	-55.0137	6.11908E+43	2465	13472	0.859754	33.4279
64.645904	-57.2796	1.32246E+44	5778	4066	0.860375	20.5069
342.29846	-44.4718	1.73342E+43	37020	4966	0.860773	5.8011
73.841197	-53.2744	1.99554E+43	17371	3930	0.862314	11.7811
36.529147	-4.76203	2.12418E+43	55395	9368	0.864801	5.25192
74.127332	-51.3073	5.67276E+42	4094	13474	0.866626	18.1271
150.06758	2.62349	2.6161E+43	40195	8494	0.867296	6.73166
15.698373	-49.2873	6.03708E+43	7	14022	0.87479	188.129
15.751735	-49.2856	5.1888E+43	7	14022	0.87479	188.129
15.716403	-49.2725	1.15626E+43	7	14022	0.87479	188.129
15.723476	-49.2722	1.20548E+43	7	14022	0.87479	188.129
15.684755	-49.2546	2.21039E+43	7	14022	0.87479	188.129
15.771570	-49.2735	1.07757E+43	7	14022	0.87479	188.129
15.730388	-49.2614	3.29701E+43	7	14022	0.87479	188.129
15.734847	-49.2677	7.27744E+42	7	14022	0.87479	188.129
15.780841	-49.2463	1.60535E+43	7	14022	0.87479	188.129
15.670166	-49.2334	1.21122E+43	7	14023	0.87479	188.129
69.49899	-54.4022	2.30247E+43	7275	12259	0.876439	7.14354

77.265835	-53.6346	2.33005E+43	28266	9432	0.879762	12.4675
34.95566	-5.13634	2.30028E+43	4610	13374	0.882163	20.3391
34.926115	-5.15482	2.01775E+43	4610	13374	0.882163	20.3391
34.937785	-5.13686	1.91017E+43	4610	13374	0.882163	20.3391
150.51015	2.10276	1.48797E+43	25503	15229	0.885118	7.90629
150.50216	2.12584	6.24942E+42	25503	15229	0.885118	7.90629
150.48843	2.15047	2.28857E+43	25503	8000	0.885118	7.90629
66.493645	-54.9760	5.99574E+43	37913	13472	0.893167	5.89263
73.519608	-53.3171	2.11141E+43	49940	3930	0.896508	5.41973
73.533963	-53.3108	6.43497E+42	49940	3930	0.896508	5.41973
8.2888880	-43.4160	1.53881E+43	44796	7017	0.89884	5.86212